

Fixation of transparent bone pins with photocuring biocomposites

*Original*

Fixation of transparent bone pins with photocuring biocomposites / Wicaksono, G.; Toni, F.; Wei Feng Tok, L.; Jun Ting Thng, J.; Solic, I.; Singh, M.; Djordjevic, I.; Baino, F.; Steele, T. W. J.. - In: ACS BIOMATERIALS SCIENCE & ENGINEERING. - ISSN 2373-9878. - ELETTRONICO. - 7:9(2021), pp. 4463-4473. [[10.1021/acsbiomaterials.1c00473](https://doi.org/10.1021/acsbiomaterials.1c00473)]

*Availability:*

This version is available at: 11583/2937034 since: 2021-11-11T10:58:04Z

*Publisher:*

American Chemical Society

*Published*

DOI:[10.1021/acsbiomaterials.1c00473](https://doi.org/10.1021/acsbiomaterials.1c00473)

*Terms of use:*

This article is made available under terms and conditions as specified in the corresponding bibliographic description in the repository

*Publisher copyright*

ACS postprint/Author's Accepted Manuscript

This document is the Accepted Manuscript version of a Published Work that appeared in final form in ACS BIOMATERIALS SCIENCE & ENGINEERING, copyright © American Chemical Society after peer review and technical editing by the publisher. To access the final edited and published work see <http://dx.doi.org/10.1021/acsbiomaterials.1c00473>.

(Article begins on next page)

1 **Fixation of transparent bone pins with photocuring biocomposites**

2 Gautama Wicaksono<sup>1</sup>, Felicia Toni<sup>1</sup>, Leonard Wei Feng Tok<sup>1</sup>, Jeanette Jun Ting Thng<sup>1</sup>, Ivan

3 Šolić<sup>1</sup>, Manisha Singh<sup>1</sup>, Ivan Djordjevic<sup>1</sup>, Francesco Baino<sup>2</sup>, Terry W. J. Steele\*<sup>1</sup>

4 <sup>1</sup>School of Materials Science and Engineering (MSE), Nanyang Technological University

5 (NTU), Singapore 639798.

6 <sup>2</sup>Institute of Materials Physics and Engineering, Department of Applied Science and

7 Technology, Politecnico di Torino, Torino, Italy.

8 \*Corresponding author: Terry W. J. Steele (e-mail: [wjsteele@ntu.edu.sg](mailto:wjsteele@ntu.edu.sg))

9

10

11

12

13

14

15

16

17

18

19

20

21  
22  
23  
24  
25  
26  
27  
28  
29  
30  
31  
32  
33  
34  
35  
36  
37  
38  
39  
40  
41  
42  
43

## ABSTRACT

Bone fractures are in need of rapid fixation methods, but current strategies are limited to metal pins and screws, which necessitate secondary surgeries upon removal. New techniques are sought to avoid surgical revisions, while maintaining or improving fixation speed. Herein, a method of bone fixation is proposed with transparent biopolymers anchored in place via light-activated, biocomposites based on expanding CaproGlu bioadhesives. The transparent biopolymers serve as a UV light guide for the activation of CaproGlu biocomposites that results in evolution of molecular nitrogen (from diazirine photolysis), simultaneously expanding the covalently crosslinked matrix. Osseointegration additives of hydroxyapatite or Bioglass 45S5 yield a biocomposite matrix with increased stiffness and pull-out strength. The structure-property relationships of UV joules dose, pin diameter, and biocomposite additives are assessed with respect to apparent viscosity, shear modulus, spatiotemporal pin curing, and lap-shear adhesion. Finally, a model system is proposed based on *ex vivo* investigation with bone tissue for the exploration and optimization of UV-active transparent biopolymer fixation.

**KEY WORDS:** *Bone implant fixation, polymer bioadhesive, bone biocomposite, hydroxyapatite, Bioglass.*

## 1. INTRODUCTION

44 Bone fractures are rising globally with a projected 7.5 million clinical cases by 2025 in USA  
45 and Europe, in part due to an ageing population and active lifestyles. Despite the advances in  
46 orthopaedic surgery, the rate of surgical revision and non-union fracture is alarmingly high:  
47 10 to 50% of cases end up with failures characterized by revision surgery or non-union  
48 fracture.<sup>1</sup> One of the major reasons for unsuccessful bone tissue repair is suppression of blood  
49 supply to the tissue that in most cases results in non-union of the bone due to osteonecrosis,  
50 bone resorption and ischemia.<sup>1</sup> Biomaterials design for bone regeneration requires  
51 biomimetic approach from nano- to micro-scale. Properties of composite biomaterials like  
52 biocompatibility, degradation rate and the type/characteristics of bioactive inclusions  
53 embedded in the matrix have to be tailored to allow osseointegration in initial stage of  
54 healing.<sup>2</sup> Bone remodelling (i.e. healing) is a multi-phase process where biomechanical  
55 properties undergo dynamic change correlated to bone mineral density<sup>3-5</sup> as Young's modulus  
56 for human granulation tissue is ~0.5 MPa and rises up to 20 GPa for mature bone.<sup>6</sup> The  
57 variation of callus mechanical moduli through the multi-phase healing process can be in the  
58 range of 20-6000 MPa.<sup>7</sup> In case of implant-assisted fracture repair, the callus formation  
59 begins at the implant surface; the tissue formation is highly responsive to interfacial /  
60 mechanical properties of the implant and the process is known as contact osteogenesis.<sup>8</sup> Due  
61 to complexity of bone tissue, the development of biomaterials that would mimic bone  
62 biomechanics and structure to facilitate fracture healing still presents an unmet clinical need.<sup>9</sup>

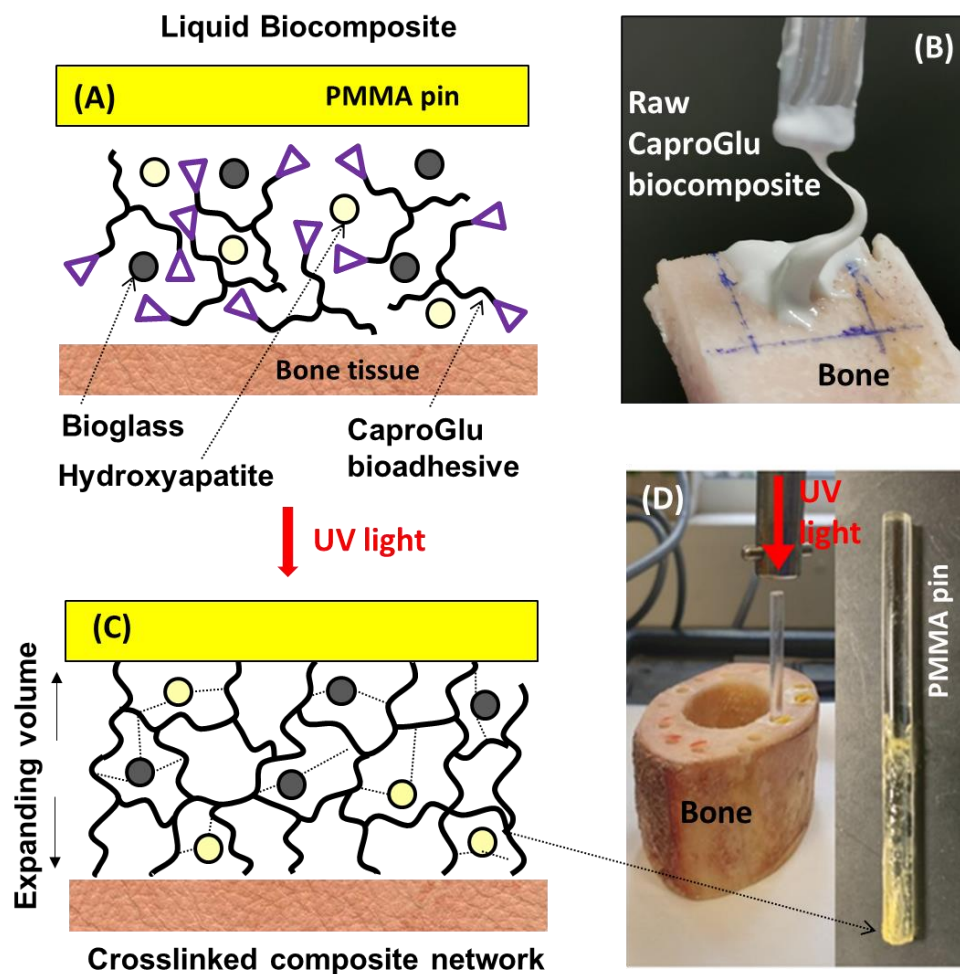
63 Bone fixation screws and pins have been employed in clinical practice for decades. Apart  
64 from standard metallic implants,<sup>10</sup> bone fixation is also performed with biodegradable plates  
65 and screws that offer less invasive approaches.<sup>11-12</sup> Recently reported clinical trials indicate  
66 that bioresorbable polymer (polycaprolactone, PCL; poly(lactic acid), PLA) and permanent  
67 implants (metallic) are equally safe and effective for non-load-bearing bone reconstruction.<sup>13</sup>  
68 Resorbable implants eliminate the need for secondary surgery which is required for metallic

69 implants after tissue healing is completed. The bone microenvironment repair relies on  
70 sensitive bone / implant interface<sup>14</sup> that is disrupted by compression (force-mediated) fixation  
71 that causes peri-implant bone damage up to 0.9 mm in radial direction from the implant.<sup>15</sup>  
72 This issue compromises the primary implant stability and should be addressed by non-  
73 invasive, biodegradable fixation formulations that combine principles of surgical adhesion  
74 and tissue engineering.

75 Over the recent years we have developed a diazirine-grafted polycaprolactone polyol (named  
76 CaproGlu) hydrophobic, liquid bioadhesive that can be mixed with bone mineral  
77 hydroxyapatite to yield viscous liquid biocomposite (**Scheme 1A,B**).<sup>16-17</sup> The CaproGlu  
78 platform is based on polycaprolactone triol or tetrol (PCLT) grafted with  
79 trifluoromethylphenyl diazirine as a surgical adhesive.<sup>18</sup> UV activation of diazirine generates  
80 carbene that rapidly crosslinks with release of molecular nitrogen that causes a >200%  
81 volumetric expansion and pressures that could exceed 200 kPa (**Scheme 1C**).<sup>19</sup> Carbene  
82 covalently inserts non-specifically causing both internal and interfacial crosslinking that  
83 immobilizes bone implants (**Scheme 1D**).<sup>17</sup> Due to known biodegradation and  
84 biocompatibility of polycaprolactone biomaterials, CaproGlu-based biocomposite bone  
85 fixation formulation presents a new strategy for fixation of transparent bone pins crosslinked  
86 with low energy UV light. To the best of the authors' knowledge, there has been no prior  
87 research on utilizing photoactive, polycaprolactone-based biocomposite that mediates non-  
88 invasive fixation of light-activated bone pins.

89 In this paper for the first time, we describe the bone fixation with UV-active bone  
90 biocomposite based on bioactive particles, namely hydroxyapatite (both micro- and nano-  
91 particles) and glass microparticles. CaproGlu biocomposite is activated on-demand via a  
92 novel fibre-optic pin (polymethyl methacrylate; PMMA) platform (**Scheme 1C,D**).  
93 Transparent PMMA is used only as a model that simulates bone fixation by transparent,

94 commercially available polylactide pins (e.g. Inion CPS™).<sup>20</sup> Described bone biocomposite  
 95 integrates tissue engineering approach with bone implant (pin) fixation where the  
 96 biocomposite serves as a temporary support that evenly transfers stress from the healing  
 97 tissue to the immobilized pin. The design of fibre-optic orthopaedic implant is directed by the  
 98 following key requirements: (i) Biocomposite liquid conforms to the drilled gap, where  
 99 activation causes volume expansion that solidifies and fills complex voids and geometries;  
 100 (ii) Biocomposite is produced from biodegradable materials that induce osseointegration; (iii)  
 101 Non-exothermic *in situ* crosslinking by exposure to non-invasive, low energy UV light with  
 102 adhesion properties that allow flexibility towards specific bone reconstructive surgery; and  
 103 (iv) Transparent fibre-optic pin made from PMMA allowing delivery of UV light that  
 104 crosslinks CaproGlu component of biocomposite.



105

106 **Scheme 1.** Demonstration of light activation of transparent bone pins with the aid of  
107 CaproGlu biocomposite formulation. (A) Composite is produced by mixing diazirine-grafted  
108 polycaprolactone (CaproGlu; branched polyol with diazirine end-groups, symbolically  
109 presented as triangle shapes) with solid additives: Bioglass (45S5) and hydroxyapatite. (B)  
110 Representative paste-like biocomposite formulation prior to UV activation. (C) UV light (365  
111 nm) transmitted through light-transparent PMMA pin activates diazirine groups and turn  
112 them into carbene for subsequent crosslinking of biocomposite at PMMA-bone interface;  
113 diazirine photolytic degradation produces molecular nitrogen bubbles that expand  
114 biocomposite and cause locking pressure for pin fixation. (D) *Ex-vivo* experimental setup to  
115 investigate light activation of transparent bone pins with the aid of expendable, UV-active  
116 biocomposite for mechanical locking at the bone / pin interface.

117

118 It is hypothesized that the thickness of bone-implant (pin) interface should be kept below 0.2  
119 mm in order to ensure sufficient light transmission and UVA energy distribution and to  
120 generate sufficient interfacial crosslinking for compressive stresses that are sustained through  
121 the biocomposite matrix. The results herein present the preliminary investigations of the  
122 model system towards developing of new methods of bone fixation with non-metallic  
123 implants.

124

## 125 **2. MATERIALS AND METHODS**

### 126 **2.1 Synthesis of CaproGlu bioadhesive and biocomposite preparation methodology**

127 The detailed synthesis procedure of CaproGlu has been described in a previous publication.<sup>16</sup>

128 In brief, polycaprolactone triol (CAPA 3031, 300 Da, Perstorp, Sweden) and diazirine-  
129 bromide (TCI, Japan) are mixed in PCLT/diazirine molar ratio of 1/1 to yield 50% diazirine  
130 conjugation. Reactants are dissolved in dioxane and allowed to react in the presence of silver  
131 oxide (Ag<sub>2</sub>O) and molecular sieve for 72 h at room temperature under nitrogen atmosphere.

132 Filtered product is precipitated in deionized water and centrifuged; the water-dioxane  
133 supernatant is discarded and the PCLT-D conjugate product (viscous pale-yellow transparent  
134 liquid) is further washed 3 times with water and centrifuged. PCLT-D formulations are  
135 lyophilized for 24 h and characterized with  $^1\text{H}$  NMR to calculate the conjugation (grafting)  
136 percentage (Bruker Avance; 400 MHz). Refractive index (RI) of purified CaproGlu is  
137 measured by Mettler Toledo portable refractometer 30GS at room temperature, and RI  
138 estimation of CaproGlu bioadhesive composites are performed using Lorentz-Lorenz  
139 equation for rule of mixtures.<sup>21</sup> CaproGlu bioadhesive composites are prepared by directly  
140 mixing the additive powder into the liquid CaproGlu formulation. Hydroxyapatite  
141 nanopowder (hereafter referred as HNP), <200 nm particle size are purchased from Sigma  
142 Aldrich. Hydroxyapatite coarse powder (hereafter referred as HMP), ultrapure grade ( $10 \pm$   
143  $2.0 \mu\text{m}$  particle size) were purchased from Sigma Aldrich. Bioglass 45S5 powder, <32 nm  
144 particle size (hereafter referred as BG), is synthesized by melt-quenching process followed by  
145 milling and sieving, as previously described.<sup>22</sup>

## 146 **2.2 Photorheometry measurements**

147 Rheometry measurements are conducted with Anton Paar Physica MCR 102 rheometer fitted  
148 with UV transparent glass plate. The applied UV intensity (365 nm) is calibrated to  $100 \text{ mW}$   
149  $\text{cm}^{-2}$  with an IL 1400 Radiometer through handheld UV LEDs or by Thorlabs SOLIS-365C  
150 High Power LED. Rheology tests are performed using parallel plate geometry with probe  
151 diameter 10 mm, on 0.1, 0.2 and 0.4 mm measuring gaps. Apparent viscosity is evaluated via  
152 rotational rheology with shear rate  $10 \text{ s}^{-1}$  for 60 seconds. The storage modulus ( $G'$ ) and loss  
153 modulus ( $G''$ ) are evaluated during dynamic oscillatory rheology with amplitude of 1% and  
154 frequency of 10 Hz for 160 seconds; UV irradiation is performed between  $t = 30 \text{ s}$  and  $t =$   
155  $130 \text{ s}$  to achieve total UV dose of 10 J. Amplitude sweep of 1-1000% shear strain are  
156 performed onto the cured sample to evaluate yield stress and strain.



157 **2.3 PMMA Optical Fiber and surface area evaluation**

158 Optical fiber-grade PMMA rods of diameters 1 mm, 1.5 mm, 2 mm, and 3 mm were  
159 purchased from Edmund Optics Pte Ltd. The fibres are cut into 3 cm, 5 cm, or 7 cm lengths  
160 and their ends are polished using 120-grit sandpaper. Cured biocomposites on the optical  
161 fibers are taken for image analysis using ImageJ software. The images are split into RGB  
162 channels and thresholded to identify and count the ratio of pixels representing yellow-cured  
163 biocomposite against the total area. For the purpose of analysis, the cured area is split into 10  
164 identical lengths along the direction of UV curing and the cured pixel ratio is calculated per  
165 section. The resulting % cured versus UV curing distance is fitted according Gauss  
166 probability distribution.

167 **2.4 Shear adhesion test on ex vivo bovine femur bones**

168 Bovine femur cortical bone samples are prepared at length of ~4 cm. Holes are drilled  
169 through the outer cortical bone with diameter of 3.4 mm; only 3 mm diameter optical fibers  
170 are tested, and the extra 0.4 mm allows ~0.2 mm thickness of biocomposite coating.  
171 Approximately 15 mg of adhesive is applied at 2.5 cm of the fiber length then inserted into  
172 drilled hole, and any excess adhesive outside the bone is removed. UV is applied at intensity  
173  $100 \text{ mW cm}^{-2}$  for 5 minutes (30 J) through the fibre optic; excess dose is required to  
174 compensate for irregular curing efficiencies. Load is applied to the photocured PMMA pin in  
175 the axial direction, and the shear stress calculated with respect to surface area and 0.2 mm  
176 coating thickness with the aid of a modified tensile tester (Chatillon Force Measurement  
177 Products, USA) at the strain rate of  $3 \text{ mm min}^{-1}$  with 50 N capacity force cell ( $\pm 0.25\%$   
178 resolution).

179 **2.5 SEM/EDX analysis**

180 CaproGlu is manually mixed with BG, HNP and HMP particles (10% w/w; solid/CaproGlu)  
181 and applied in thin layer (~50 mg) between PET sheets (sandwich structure) and cured with  
182 10 J of UV. PETs are separated with cured CaproGlu composite on both sheets. Composite +  
183 PET is cut in 2 x 2 mm squares for SEM/EDX analysis with JEOL 5500LV electron  
184 microscope. Samples are subjected to platinum coating (90 s, chamber pressure <5 Pa at 20  
185 mA). Images are obtained by JSM 5510 SEM at an acceleration voltage of 5–20 kV and a  
186 working distance of 15 mm. The composition of the composites is analysed by EDX using an  
187 Oxford Inca 200 EDX detector under low Vacuum and a measuring time of 300 s. Pore size  
188 distribution analysis is performed with ImageJ software by measuring the pore sizes recorded  
189 over the  $7.5 \times 10^{-3} \text{ cm}^2$  area. The SEM images are thresholded to outline the porous  
190 morphology and the resulting pore sizes are measured using the built-in particle analysis  
191 function.

## 192 **2.6 Data analysis**

193 All data processing, plotting and curve fitting are performed using OriginPro 2020 software.  
194 SEM Image analysis are performed using Fiji ImageJ 1.52. All biocomposite  
195 characterizations are performed in triplicate. One-way ANOVA statistical analysis is  
196 performed by Tukey's comparison and  $P < 0.05$  was set as significant in all the tests.

197

## 198 **3. RESULTS AND DISCUSSION**

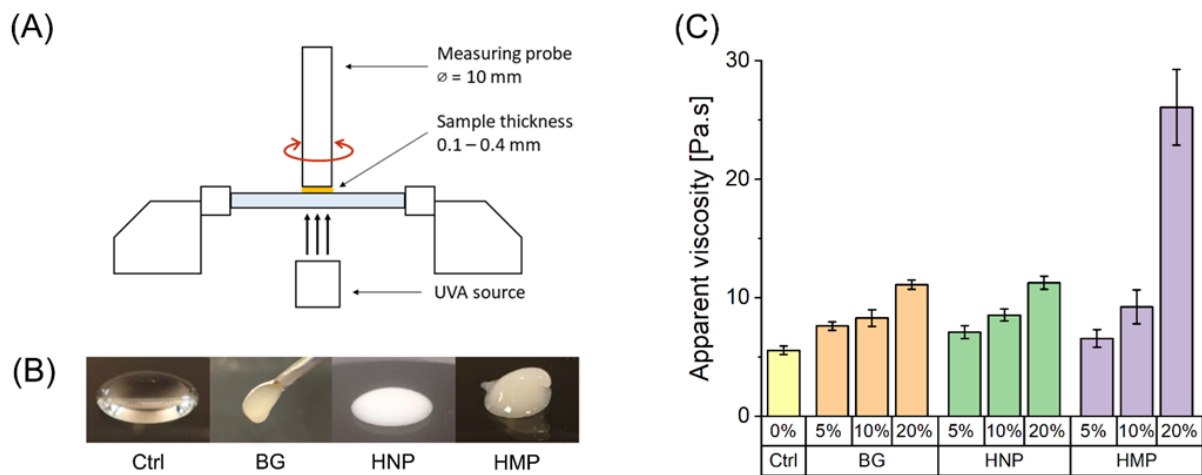
199 Nine biocomposite formulations (3 additives at 3 concentrations each) are evaluated for light  
200 activated fixation of transparent plastic implants. Several inorganic additives are available for  
201 inducing osseointegration, however we have limited the structure property relationship  
202 parameters to two different types of inorganic particles: hydroxyapatite and silica-based  
203 bioactive glass<sup>23-25</sup> (BG; 45S5 composition). In order to demonstrate the relationship between

204 mechanical properties and the size of inorganic solid phase, we report the investigation of  
205 particles in following sizes: hydroxyapatite nanoparticles and microparticles (HNP < 200 nm  
206 and HMP =  $10 \pm 2.0 \mu\text{m}$ , respectively) and bioactive glass (BG <  $32 \mu\text{m}$ ). Additive loading is  
207 hypothesized to improve the adhesive stiffness and shear adhesion strength, so each additive  
208 formulation is evaluated from 5 – 20% w/w loading. Below 5% observed no additional  
209 increase in shear modulus (vs. neat CaproGlu) and above 20% yield viscous pastes with  
210 viscosity above 10 Pa.s (**Fig. 1**). All biocomposites are evaluated by real-time  
211 photorheometry, in a multi-step protocol that yields a robust analysis of uncured liquid, joule-  
212 dependent viscoelasticity, gelation time, and strain-dependent shear modulus. The latter  
213 correlates to lap shear adhesion assuming cohesive failure. Each photorheometry experiment  
214 is done in triplicate. Three thickness profiles (0.1, 0.2, and 0.4 mm) evaluate effects of UV  
215 light attenuation through the biocomposite for total of (9 biocomposites x 3 thickness profiles  
216 x triplicates) 81 independent rheometer evaluations. Four diameters of UV transparent  
217 polymethacrylate (PMMA) are evaluated as light-transparent pins. Optical fiber-grade  
218 poly(methyl methacrylate) PMMA is required for sufficient UV transparency (hobby grades  
219 were UV opaque, data not shown). PMMA serves as a model bone pin material, as it is UV  
220 transparent, readily available, and having an elastic modulus slightly softer than cortical bone  
221 at 3 GPa.<sup>26 27</sup> In order to assess the lap shear adhesion at the bone implant interface, fresh *ex*  
222 *vivo* bovine femur bones are drilled at 3.4 mm diameter (pin diameter + 0.4 mm) and excess  
223 biocomposite is applied into a bone pin mimic, inserted into the hole. As the adhesive  
224 composite requires UV activation, the optical fiber-grade PMMA serves as the model  
225 transparent pin material.

### 226 **3.1 Real-time photorheometry of composites**

227 Biocomposites of liquid CaproGlu and three inorganic additives are prepared in three weight  
228 ratios. A multistep photorheometry protocol evaluates the biocomposites at all stages of the

229 curing from liquid, UV-induced gelation, to determining the strain-dependent modulus and  
 230 maximum shear strain (prior to *ex vivo* experiment) with the following framework; i) parallel  
 231 plate rotational shear ( $\eta_{app}$  UV off, 60 s), ii) oscillatory ( $G''/G'$  for 30 s UV off + 100 s UV  
 232 on + 30 s UV off), iii) followed by an amplitude sweep ( $G''/G'$  from 1 – 1000%, UV off).  
 233 The photorheometry setup is shown in **Fig. 1A**, with UV source below the biocomposite  
 234 sample placed on a quartz surface. **Fig. 1B** shows pictures of the various composites tested:  
 235 pure CaproGlu is translucent while CaproGlu mixed with BG, HNP, and HMP additives are  
 236 opaque from particle light scattering. **Fig. 1C** shows the apparent viscosity as function of  
 237 additive concentration, with values listed in **Table 1**.



238  
 239 **Figure 1.** Photorheometry experimental setup: (A) Schematics presentation of rheometer  
 240 fitted with light-transparent base with outlined dimension parameters. (B) Close-up pictures,  
 241 from left to right: pure CaproGlu, CaproGlu + 20% BG, CaproGlu + 20% HNP, CaproGlu +  
 242 20% HMP. (C) Summary of viscosity values measured for biocomposites as a function of  
 243 additive concentration in comparison to pure CaproGlu (control; 0%).

244

245 **Table 1.** Apparent viscosity (Pa.s) of composites: shear <sup>rate</sup> 10 s<sup>-1</sup>; base-probe thickness 0.2  
 246 mm.

Additive concentration	Bioglass 45S5 (BG)	Hydroxyapatite nanopowder (HNP)	Hydroxyapatite coarse powder (HMP)
0% (control)	5.55 ± 0.37		

5%	$7.60 \pm 0.36$	$7.10 \pm 0.54$	$6.56 \pm 0.75$
10%	$8.29 \pm 0.70$	$8.54 \pm 0.51$	$9.22 \pm 1.42$
20%	$11.1 \pm 0.40$	$11.3 \pm 0.54$	$26.1 \pm 3.21$

247

248 CaproGlu by itself (no additives) has average viscosity of 5 Pa.s. Inclusion of both BG and  
 249 HNP additives up to 10% still results in viscosity lower than 10 Pa.s, and subsequent addition  
 250 of solid particles increase the viscosity significantly. In particular, addition of 20% HMP  
 251 displays considerable increases, likely surpassing the contact percolation threshold. Most of  
 252 the uncured formulations display aspects of a Bingham plastic and are able to coat surfaces  
 253 with thickness greater than 0.2 mm under the force of gravity.

254 Photorheometry is performed using 365 nm wavelength (defined here as UV light) at  
 255 intensity of  $100 \text{ mW}\cdot\text{cm}^{-2}$  for 100 seconds, for a total dose of  $10 \text{ J}\cdot\text{cm}^{-2}$ . Before UV curing,  
 256 the sample is pre-sheared for 30 seconds under oscillatory rheometry, which disrupts any  
 257 structures, placing the biocomposite in viscous liquid state where  $G'' > G'$ . During UV  
 258 exposure, CaproGlu crosslinks, evidenced by an increase in  $G'$  (storage modulus). The  
 259 sample turns from viscous liquid to viscoelastic solid, represented by gelation point  $G' = G''$   
 260 (see **Fig. 2A**): an irreversible transition from liquid to elastomeric material consistency. After  
 261 curing, the biocomposites are crosslinked and  $G' \gg G''$ . **Fig. 2A** shows a representative plot  
 262 of  $G''$  and  $G'$  versus curing time, comparing the properties of pure CaproGlu vs CaproGlu  
 263 with 20% BG additive, at 0.1 mm thickness. **Fig. 2B** displays a comparison of all three  
 264 additives at 20% loading, 0.2 mm thickness. An increase of  $G'$  values with BG microparticles  
 265 after curing as a function of loading is presented in **Fig. 2C** and a plot of  $G'$  vs. thickness for  
 266 BG, HNP and HMP is shown in **Fig. 2D**. **Table 2** lists complete values of  $G'$  after 10 J of UV  
 267 curing. In addition, the process of crosslinking CaproGlu generates the maximum force of  
 268 expansion which can be detected by the rheometer probe (**Table S1**). The values are

269 dependent on the base-probe distance and the maximum recorded force is  $52 \pm 6$  kPa for 0.1  
 270 mm distance. The expansion force drops for an order of magnitude with increase of distance  
 271 to 0.4 mm (**Table S1**). Even at the maximum value, the expansion force caused by CaproGlu  
 272 crosslinking reaction is significantly lower than rupture stress measured for adult cranial  
 273 human bone (100 MPa order of magnitude).<sup>28</sup>

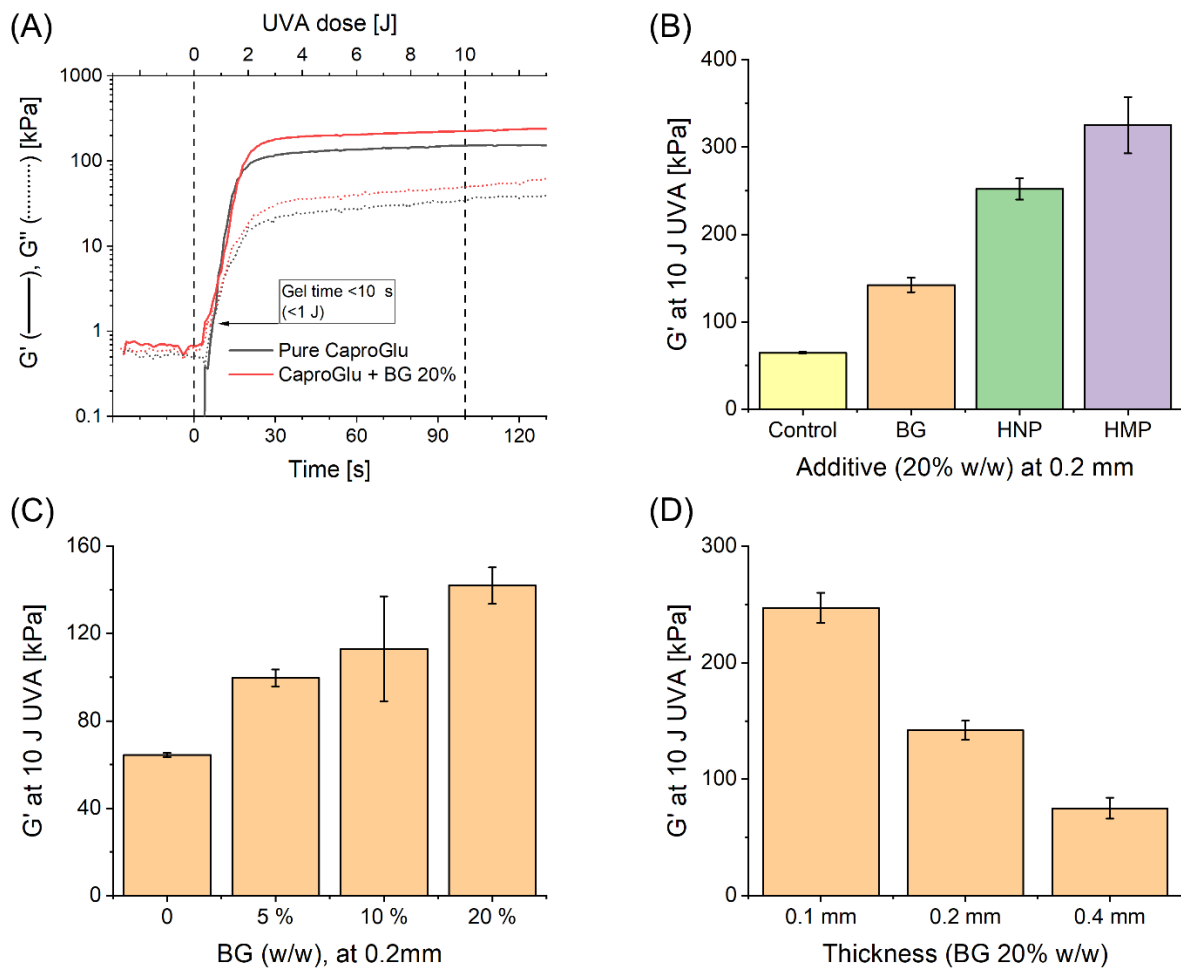


**Figure 2.** Photoreological properties of CaproGlu biocomposite formulations: **(A)** Plot of biocomposite photocuring showing the evolution of  $G'$  and  $G''$  versus UV curing time, representative for pure CaproGlu vs Caproglu + 20% BG. **(B)** Comparison of  $G'$  after curing as function of additive type, representative for 20% (w/w) loading and 0.2 mm probe-base gap. **(C)** Comparison of  $G'$  after curing as function of additive loading, representative for BG and 0.2 mm thickness. **(D)** Comparison of  $G'$  after curing as a function of base-probe thickness, representative for BG at 20% (w/w) loading.

274

275

276

277

278

279 **Table 2.** Values of G' (storage modulus; kPa) after photocuring at total dose of 10 J.cm<sup>-2</sup>.

Measurement thickness	Additive concentration (w/w)	Bioglass 45S5 (BG)	Hydroxyapatite nanopowder (HNP)	Hydroxyapatite coarse powder (HMP)
0.1 mm	0 %	155 ± 1.75		
	5 %	171 ± 35.0	172 ± 1.95	138 ± 24.9
	10 %	241 ± 35.9	191 ± 8.0	176 ± 27.6
	20 %	247 ± 12.9	250 ± 17.1	467 ± 22.1
0.2 mm	0 %	64.4 ± 0.93		
	5 %	99.6 ± 3.89	167 ± 14.6	66.3 ± 32.5
	10 %	113 ± 24	199 ± 12.6	112 ± 13.8
	20 %	142 ± 8.29	252 ± 12.2	325 ± 32
0.4 mm	0 %	49.5 ± 3.65		
	5 %	31.4 ± 1.58	54.1 ± 0.22	48.6 ± 6.67
	10 %	74.6 ± 3.56	61.2 ± 4.51	37.6 ± 2.45
	20 %	75.0 ± 8.89	67.3 ± 5.26	16.5 ± 5.02

280

281 Note that the HMP microparticles appear to have the highest light attenuation as judged by G'

282 from 0.1 to 0.4 thickness. The rheometer probe evaluates the biocomposite surface with the

283 least amount of light exposure. Taken together, the results suggest that thickness should be

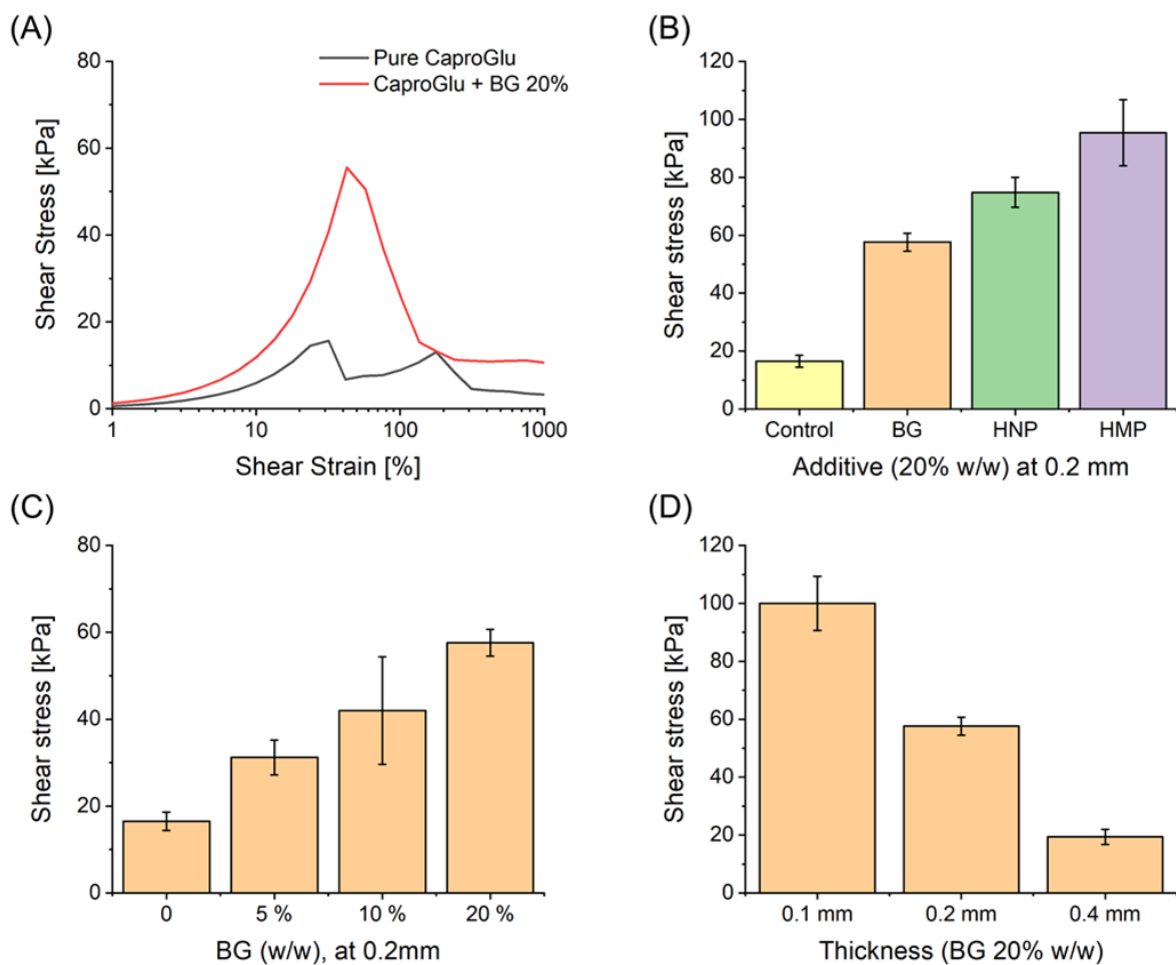
284 kept at 0.2 mm or smaller in order to limit gradients. Gelation point is reached within first 10

285 seconds of UV curing for sample thickness of 0.1 mm, up to 34 s for 0.2 mm, and 82 s for 0.4

286 mm (*Supplementary information: Fig. S1-S3*). It is shown that osseointegration additives can

287 improve modulus and yield stress of CaproGlu without compromising gelation time/ gelation  
288 dose, therefore granting user control on the application of the adhesive.

289 Performing amplitude sweep on the UV-cured composites allows to plot a dynamic stress vs  
290 strain plot as shown in **Fig. 3A**, representative for pure CaproGlu vs CaproGlu with 20% BG  
291 additive, at 20% loading. **Fig. 3B** displays the comparison for additives at 20% loading, 0.2  
292 mm thickness. Addition of BG up to 20% by weight greatly increases the yield stress, from  
293 16 kPa to 58 kPa, while addition of HMP increases it up to 95 kPa. Additives loading  
294 improves stress at break, representative for BG at 0.2 mm thickness (**Fig. 3C**). The stress at  
295 yield point (break) decreases with sample thickness, as shown in **Fig. 3D** for all additives  
296 used in experiments. The complete values of stress at break are listed in **Table 3**. This points  
297 to evidence of decreasing the effectiveness of UV curing with increasing thickness.



298



299 **Figure 3.** Rheological amplitude sweep profile of CaproGlu biocomposites: (A) Plot of  
 300 dynamic stress vs strain of photocured biocomposite, representative for pure CaproGlu  
 301 (control) vs Caproglu + 20% BG. (B) Comparison of stress at break as function of additive  
 302 type, representative for 20% (w/w) loading and 0.2 mm thickness. (C) Comparison of stress  
 303 at break as function of additive loading, representative for BG and 0.2 mm probe-base  
 304 thickness. (D) Comparison of stress at break as function of thickness, representative for BG at  
 305 20% (w/w) loading.

306

307 **Table 3.** Shear stress (kPa) of photocured composites at yield point.

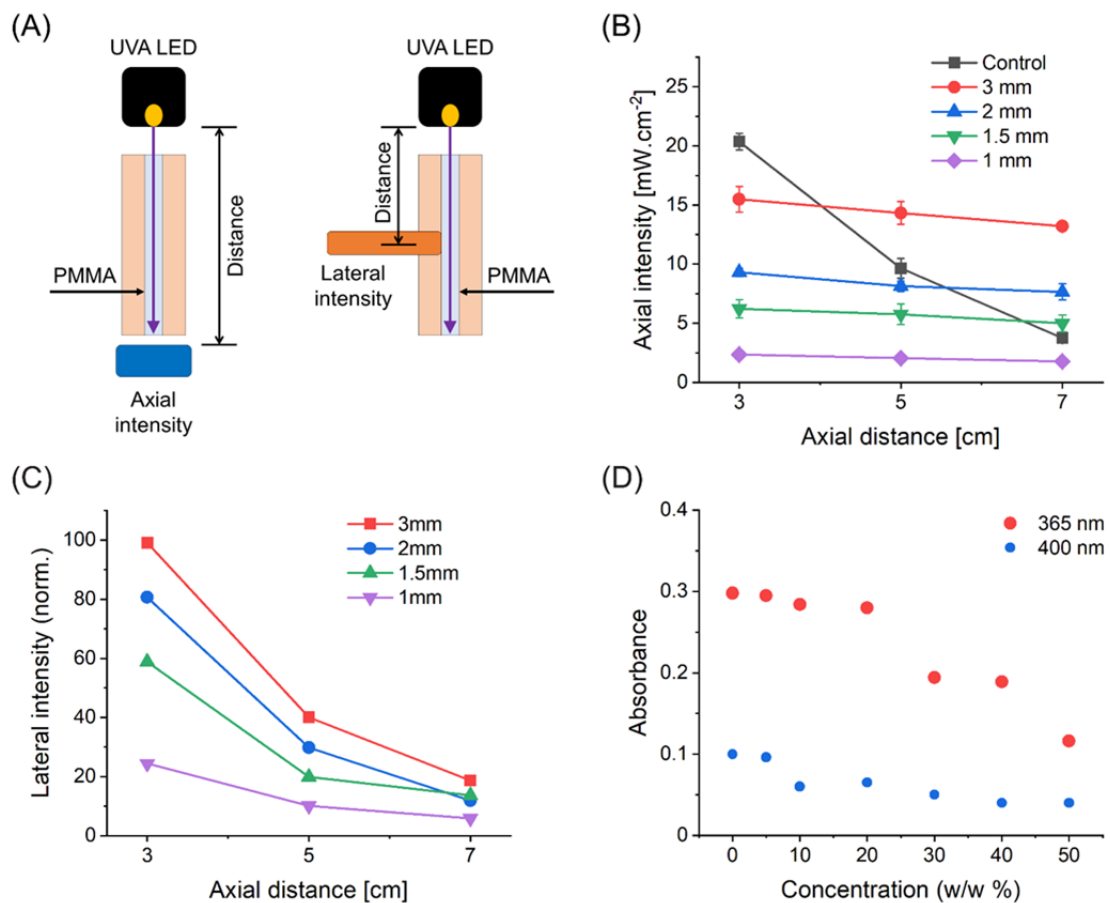
Measurement thickness	Additive concentration (w/w)	Bioglass 45S5 (BG)	Hydroxyapatite nanopowder (HNP)	Hydroxyapatite coarse powder (HMP)
0.1 mm	0 %	36.4 ± 0.33		
	5 %	56.9 ± 6.97	112 ± 2.60	71.7 ± 16.6
	10 %	78.3 ± 8.65	113 ± 4.79	84.4 ± 13.1
	20 %	100 ± 9.38	127 ± 9.51	155 ± 2.93
0.2 mm	0 %	16.5 ± 2.11		
	5 %	31.2 ± 4.02	88.7 ± 3.79	40.7 ± 20.0
	10 %	42.0 ± 12.4	85.6 ± 5.12	56.4 ± 21.5
	20 %	57.6 ± 3.1	74.8 ± 5.14	95.4 ± 11.4
0.4 mm	0 %	12.1 ± 1.52		
	5 %	9.10 ± 0.75	20.5 ± 0.66	18.8 ± 2.18
	10 %	31.3 ± 0.56	21.8 ± 2.02	12.2 ± 1.65
	20 %	19.4 ± 2.62	21.8 ± 1.71	1.78 ± 0.75

308

### 309 **3.2 Light transmission properties of PMMA optical fiber**

310 Optical fiber-grade PMMA of different diameters 1 mm, 1.5 mm, 2 mm, and 3 mm are cut  
 311 into different lengths 3 cm, 5 cm, and 7 cm. The UV LED is fitted to a custom 3D-printed  
 312 adapter to direct the light onto the 3mm diameter PMMA pin. Axial and lateral intensity  
 313 measurements are performed to assess pin transparency (intensity loss) and length dependent  
 314 attenuation. **Fig. 4A** shows the schematics of intensity measurement setup; for measurement

315 on axial direction, the PMMA optical fiber (pin) is placed directly between the UV torch and  
 316 the radiometer sensor. The distance from UV source to sensor equals to the optical fiber  
 317 length. For lateral direction, spectrometer is placed on the side of the PMMA optical fiber.  
 318 The result of this axial intensity measurement is plotted as a function of optical fiber length  
 319 and diameter (**Fig. 4B**). The control values used are intensity reading through air but at  
 320 different distance, and the highest intensity achieved is  $20 \text{ mW}\cdot\text{cm}^{-2}$  at 3 cm. With increasing  
 321 distance, the intensity reading reduces slightly. For lateral intensity measurement performed  
 322 using a spectrometer, the results are plotted as a normalized relative light unit (**Fig. 4C**).



323

324 **Figure 4.** Optical properties of PMMA pins: (A) Schematic presentation of UV intensity  
 325 measurement from axial and lateral directions. (B) Results of intensity measurement over the  
 326 axial direction of PMMA optical fibers (pins) as a function of distance and optical fiber  
 327 diameter; control values are measurements through air (no optical fiber). (C) Results of  
 328 intensity measurement over the lateral direction of PMMA optical fibers as function of

329 distance and optical fiber diameter. **(D)** Plot of absorbance of CaproGlu + BG at  
330 representative wavelengths of 365 nm and 400 nm, showing light attenuation as function of  
331 loading concentration.

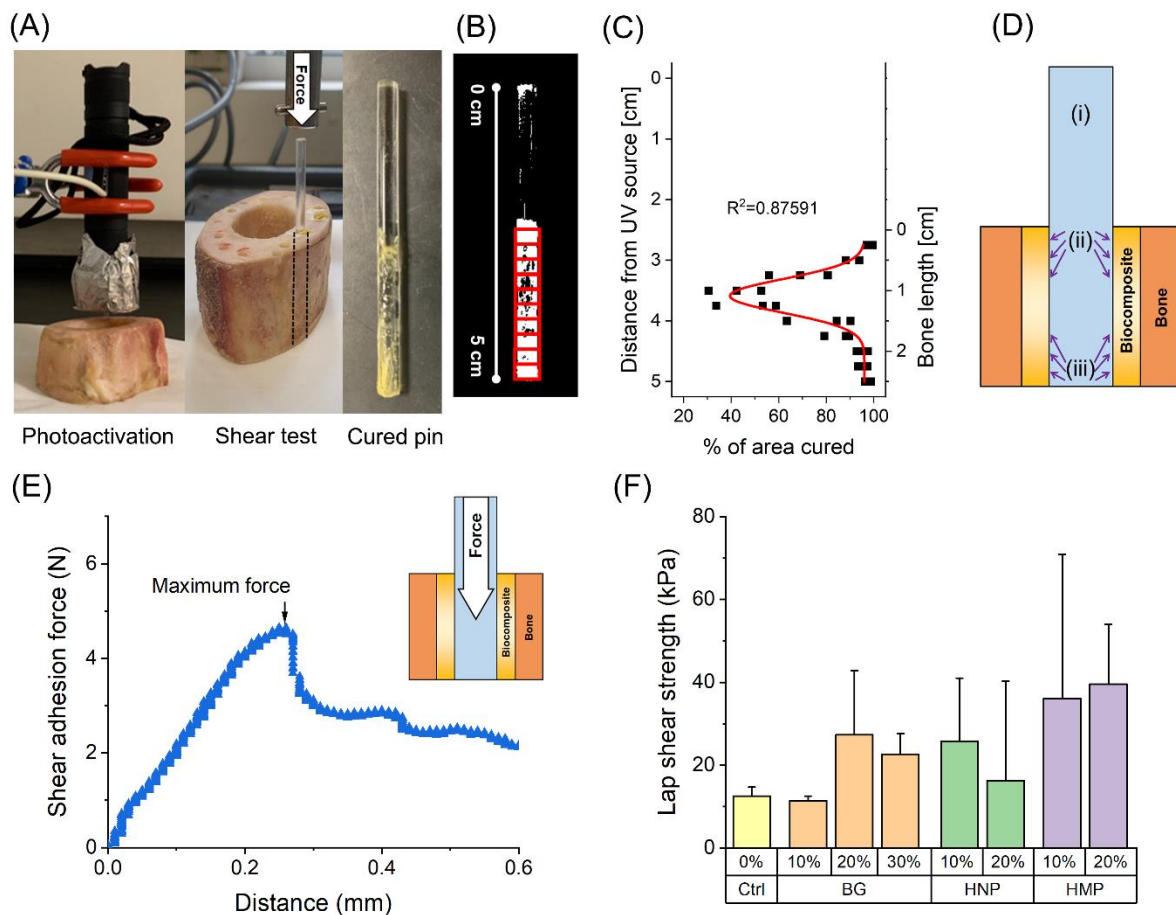
332

333 The results demonstrate that the longer the distance is, the difference between intensity  
334 readings are getting closer as dispersion starts taking effect. In both directions, the larger  
335 diameter of the optical fibers used, the more effective the light transmission becomes, and  
336 that in itself depends on the travel distance. **Fig. 4D** displays the absorbance plot of  
337 biocomposite with BG, tested at 365 nm and 400 nm, showing the light attenuation as  
338 function of loading concentration. Following the results above, for subsequent experiment  
339 results, the PMMA optical fibers with 3 mm diameter is used. Fibre length chosen is 5 cm to  
340 allow better handling of experiments.

### 341 **3.3 Lap shear testing on bovine bones and refractive index of CaproGlu biocomposites**

342 Bovine femur cortical bones are prepared with holes of  $3.4 \pm 0.1$  mm diameter drilled into the  
343 bone. Excess biocomposites (~15 mg) are applied to 2.5 cm of the length and inserted into the  
344 bone. UV activation is performed by exposing the PMMA optical fibers with UV for 5  
345 minutes (**Fig. 5A, left**). Subsequently, the cured adhesive is subjected to shear test by pushing  
346 the PMMA optical fiber using a tensile tester (**Fig. 5A, middle**). Once the PMMA optical  
347 fiber is removed, it is shown that the biocomposites are only partially cured down the length  
348 of the PMMA rod, with uncured region in the middle (**Fig. 5A, right**). An image analysis  
349 estimates the amount of surface curing through the clear to yellow biocomposite colour  
350 change (**Fig. 5B,C**), where the yellow tint is caused by diazoalkane formation.<sup>29</sup> At the  
351 air/PMMA interface, UV light is internally reflected ( $42^\circ$  critical angle, refractive index of  
352 1.49; **Fig. 5D, i**). Internal reflection no longer occurs at the CaproGlu interface because  
353 polycaprolactone (major constituent of CaproGlu) has refractive index of 1.46, similar to

354 PMMA. Diffracted UV light is therefore absorbed by the biocomposite that caused  
 355 crosslinking (**Fig. 5D, ii**), but the light flux decreases along the length, creating a gradient of  
 356 crosslinking as function of distance from UV source. Non-uniform crosslinking caused by  
 357 this effect will be addressed in future by applying more sophisticated optics than simple UVA  
 358 diode used as a proof of concept in this paper (**Fig. 5A**). Regardless of recorded non-uniform  
 359 light energy distribution (**Fig. 5C,D**) the reflection of UV on the opposite PMMA surface  
 360 creates a second virtual light source (**Fig. 5D, iii**), which is responsible for curing from the  
 361 opposite end of PMMA fiber. This explains the Gaussian distribution of biocomposite curing  
 362 between real and virtual light source as seen in **Fig. 5C**.



363  
 364 **Figure 5.** *Ex vivo* investigation of PMMA fixation by UV-activated CaproGlu biocomposite  
 365 formulations: (A) *Left*: UV-curing setup of composites on PMMA optical fiber surface,  
 366 inserted into holes drilled onto bovine femur bone. *Middle*: setup of shear test on bovine  
 367 femur bone; the fiber optic (pin) is pushed downwards, and the shear adhesion strength is

368 measured (the force direction is indicated with arrow). *Right:* the composites are cured  
369 partially inside the bone. **(B)** Analysis of cured area using image editing software ImageJ by  
370 dividing cured area into 10 segments for evaluation by ratio. **(C)** Cured area ratio is fitted to  
371 Gaussian distribution with  $R^2$  value of 0.87591. **(D)** Schematic presentation for proposed  
372 mechanism of UV curing through the PMMA fiber: (i) total internal reflection through air /  
373 PMMA medium, (ii) UV is absorbed by the biocomposite, (iii) reflection from original UV  
374 source cured the biocomposite from the opposite end of the pin. **(E)** Representative load vs  
375 distance curve of the shear test; increasing load represents the shear force experienced by  
376 cured biocomposite (*insert:* measured shear force interface). **(F)** Maximum force values from  
377 each sample is normalized against cured biocomposite area to determine lap shear strength of  
378 each biocomposite.

379

380 **Figure 5E** shows a representative result of this experiment on a pure CaproGlu as shear force  
381 reading at the pin-bone interface contributed by cured CaproGlu versus PMMA pin  
382 displacement, in the axial direction. As the optical fibers are sheared, load reading is  
383 increased until a maximum yield point. This value is normalized towards the cured area of  
384 adhesive, and the resulting value is defined as lap shear strength, listed in **Fig. 5F**. This  
385 ultimate shear stress value represents the adhesion (shear) strength of cured CaproGlu  
386 composite at the pin-bone interface. Curing surface area appears to be inversely dependent on  
387 the additive concentration. From 0-20% BG loading, over half the surface area is cured.  
388 There is ~10% surface curing for 30% loading and no observed curing for 40-50% loading,  
389 and therefore no lap shear adhesion results are available. As BG has high refractive index of  
390 1.55, it is hypothesized that the biocomposite resumes total internal reflection for >30%  
391 loading,<sup>30</sup> explaining the lack of curing. The standard deviation remains high due to the  
392 irregular nature of the adhesive's photocuring behaviour between bone and pin surface.

393 This work was inspired by previous investigations of polymer waveguides that elucidated the  
394 structure activity relationships of deep tissue light delivery, transparent biopolymers, and

395 photochemical tissue bonding.<sup>31</sup> With 900 J of visible irradiation, they demonstrated a  
396 significant bonding of 2 kPa, a 5x increase over control. PMMA herein serves as the model  
397 UV-transparent biopolymer—it is available in medical grades but is not considered  
398 resorbable. The differential refractive index at the PMMA / air interface allows total internal  
399 reflection, but this immediately changes to diffraction at the PMMA/ biocomposite interface.  
400 Diffraction allows photocuring / tissue bonding of CaproGlu (up to 40 kPa), but the light flux  
401 decreases along the length of the PMMA rod, thus causing insufficient crosslinking in the  
402 center of the implant. Reflection of UV light on the opposite PMMA surface creates a virtual  
403 light source which is responsible for curing from the opposite end of PMMA pin. It is  
404 important to note that we did not observe curing with particle loading exceeding 30% BG in  
405 the biocomposite. This shows that for the current design of photocuring with transparent  
406 biopolymers, the differential refractive index between the PMMA pin (RI = 1.49) and the  
407 biocomposite (**Table 4**) was sufficient to prevent diffraction – little to no light flux prevented  
408 CaproGlu photocuring as evident from the lack of shear adhesion forces. This partial curing  
409 causes less effective biocomposite crosslinking in the middle part of the pin; as such, the  
410 current application limits to short pins where light flux can be maintained through the length  
411 of the pin.<sup>32</sup> Ultimately, the lower crosslinking density is likely to cause faster resorption of  
412 polycaprolactone component.<sup>33</sup>

413 **Table 4.** Refractive Index (RI) estimation\* of CaproGlu Biocomposites.

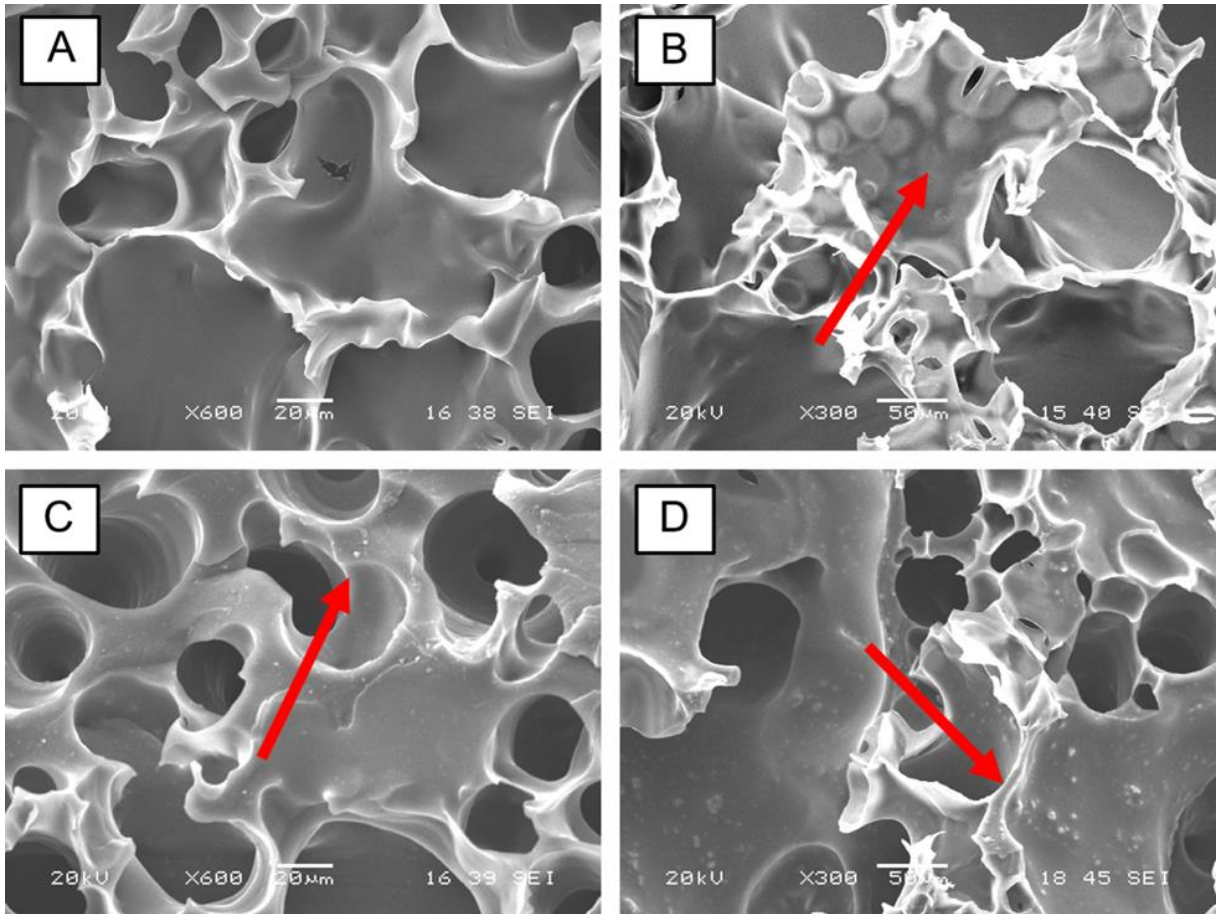
Additive concentration (w/w)	Bioglass 45S5 (BG), RI = 1.55	Hydroxyapatite (HNP & HMP), RI = 1.64
CaproGlu	1.485 ± 0.005	
5 %	1.49	1.49
10 %	1.49	1.50
20 %	1.50	1.52
30 %	1.50	1.53

414 \* *RI estimation calculated by Lorentz-Lorenz equation for rule of mixtures.*

415 While shear stresses are evaluated, we speculate the broad standard deviation results from  
416 irregular photocuring and therefore no statistical significance can be gained with respect to  
417 additive comparison. Given that the hardest part of the bone is near the surface (cortical bone),  
418 bone adhesion may not be warranted within the bone marrow and optical flux may instead be  
419 minimized within the bone marrow. Part of our future work will continue to refine the optical  
420 setup to achieve precise control over light flux to reach conclusive shear adhesion test results  
421 for UV-activated transparent bone implants.

### 422 **3.4 Scanning electron microscopy**

423 **Figure 6** shows representative scanning electron micrographs of UV-cured pure CaproGlu  
424 and composites with all 3 different additives (10%, w/w). The porous structure of all  
425 composites are the result of molecular nitrogen generation as byproduct of activation of  
426 diazirine from UV exposure. This is consistent with our previously reported results that  
427 demonstrate the same porous morphology of pure CaproGlu bioadhesive formulation.<sup>17</sup> In  
428 **Fig. 6B, 6C, and 6D**, the solid particles are shown embedded on the matrix as pointed on red  
429 arrows. EDX analysis confirms the composition of these particles belonging to that of BG,  
430 HNP and HMP (see **Table S2**). Image analysis shows the pore size distribution of each  
431 composite (**Fig. S4**) with measured pore sizes for CaproGlu (control), BG, HNP and HMP of:  
432  $43 \pm 39 \mu\text{m}$ ,  $26 \pm 19 \mu\text{m}$ ,  $41 \pm 31 \mu\text{m}$  and  $37 \pm 26 \mu\text{m}$ , respectively, which is in line of  
433 previously reported  $\sim 50 \mu\text{m}$  pore size of CaproGlu<sup>34</sup>. It should be noted that nanoparticle  
434 load (HNP) caused significantly lower pore size in comparison to both control and  
435 microparticle-embedding composite (HMP and BG; **Fig. S4**).



436

437 **Figure 6.** Morphological analysis of crosslinked CaproGlu biocomposites (UV; 10 J) by  
 438 scanning electron microscopy (SEM; arrows indicate embedded mineral particles in polymer  
 439 matrix): (A) pure CaproGlu (control). CaproGlu composites with: (B) Bioglass 45S5 (10%);  
 440 (C) hydroxyapatite nanoparticles (10%); and (D) hydroxyapatite microparticles (10%).

441

442 CaproGlu bioadhesive is designed as a solvent-free liquid pre-polymer that allows  
 443 incorporation of inorganic additives, such as hydroxyapatite and Bioglass 45S5 (**Fig. 1**).  
 444 Previous evaluation of CaproGlu composites displayed adhesion strength > 800 kPa on  
 445 cranium substrates.<sup>16</sup> Generation of molecular nitrogen as byproduct of diazirine activation  
 446 allows the initially liquid-like CaproGlu adhesive to expand into porous matrix, that fills gaps  
 447 between surfaces during photocuring, forming a solid porous matrix (**Fig. 6**). Herein, the  
 448 bone adhesion and light-activated expansion is exploited towards fixation at the implant-bone  
 449 interface.



450 As hypothesized, confining the thickness of bone-implant interface below 0.2 mm in  
451 conjunction to transparent cylindrical bone pin, compressive stresses have been generated  
452 through the adhesive matrix - a crosslinked biocomposite layer forms *in situ* at the implant-  
453 bone interface. Such unique behaviour is deemed less traumatic than compressive stresses  
454 formed by screws or pressure-fit pins: the Young's modulus of bone changes during healing  
455 in the range of 20 – 6,000 MPa<sup>7</sup>, and residual compressive stresses could form because of  
456 difference in modulus. With a crosslinked biocomposite layer acting as a mediation between  
457 implant and bone, this modulus mismatch between implant and bone can be minimized,  
458 therefore minimizing risk of complications.<sup>34-35</sup> The expanding matrix may act as a porous  
459 scaffold towards cell migration and neovascularization during remodelling stage of bone  
460 fracture healing. SEM images (**Fig. 6**) suggests that the osseointegration additive particles of  
461 Bioglass 45S5 and hydroxyapatite are embedded onto the surface of the porous matrix, which  
462 is expected to promote further bone healing.

463 Additives to liquid polymers can plasticize the matrix<sup>19, 36</sup> while solid additives improve the  
464 modulus and adhesive strength of photocured CaproGlu (**Fig. 2; Table 2**). Inorganic  
465 additives of Bioglass 45S5 and hydroxyapatite have enough fluidity to be applied by syringe,  
466 but with sufficient viscosity to allow sub-millimetre coatings to be applied. HMP additive  
467 shows the largest viscosity increase, as its  $\mu\text{m}$ -particle size is an order of magnitude larger  
468 than the HNP. As a result, its composite at 20% (w/w) have significantly increased viscosity  
469 (**Fig. 1**). Loading concentration of additives generally increases dynamic modulus of  
470 photocured biocomposite. Different types of additives result in different curing profiles (**Fig.**  
471 **S1-S3**). Photocuring itself is dependent on the penetration of UV light through the matrix,  
472 which is limited by thickness of the adhesive applied. Future designs will continue to  
473 optimize the curing through the matrix, which is one detractor of light activated bioadhesives.

474 CaproGlu composite's unique material properties sets it apart from conventional implant  
475 fixation by commercial cements, such as acrylate (i.e. Cemex<sup>®</sup>, Simplex<sup>™</sup>) or ceramic (i.e.  
476 Norian<sup>®</sup>, HydroSet<sup>®</sup>) formulations.<sup>37-39</sup> Although the clinical use of modern acrylates dates  
477 back to 1943<sup>40</sup> the next generation of fixatives seeks to avoid acrylates-based polymerization  
478 due to their unresorbable nature, immunological rejection, and further injury due to  
479 mechanical mismatch with native osteo-tissues.<sup>41</sup> Free-radical polymerization can be  
480 activated by light-based mechanisms or two-part mixing, but the bulk of these adhesives  
481 requires free radical initiators and preservatives that leach into surrounding tissues. The  
482 exothermic reactions can heat up to 100°C<sup>42</sup> if no cooling is factored into the application.  
483 Modulus can only be grossly controlled, further exacerbating tissue sensitivity.<sup>41</sup> Bone  
484 cements have the advantage of rapid fixation, but have known risks with regards to fixation /  
485 fracture failure (through accumulation of microcracks) and toxic systemic risks (bone cement  
486 implantation syndrome) caused by initiator / monomer leachates from the shrinking acrylate  
487 resins.<sup>43</sup> Calcium phosphate-based cements (CPCs) were developed to overcome acrylate  
488 impediments with major advantages over acrylates, such as osteoconductivity,  
489 osteoinductivity, bio-resorbability, and interaction with bone cells. Although CPCs are of  
490 biocompatible nature, they cannot be activated on-demand, have low mechanical strength and  
491 exhibit low interfacial adhesion with hydrated tissues.<sup>44</sup> Thus, there is still an unmet clinical  
492 need for bone-interface fixation formulations capable for non-invasive activation without  
493 exothermic crosslinking reaction and toxic leachates: features demonstrated by CaproGlu  
494 biocomposites described in this work.

495 The results reported in this paper present novel CaproGlu composite platform as potential  
496 alternative to conventional bone implant fixation formulations (i.e. acrylates, CPCs). An ideal  
497 bone implant fixation formulation should have the following properties: (1) blood and bone  
498 tissue compatibility, (2) sufficient mechanical strength to stabilize fracture, (3) straight-

499 forward and simplified application on hard-to-reach areas, and (4) bone healing mediation.<sup>45</sup>  
500 The combination of UV curing and tunable viscosity by changing additive concentrations  
501 allows greater control of adhesive application where commercial bone fixation acrylates lack  
502 (i.e. spontaneous reaction, exothermic effect, toxic leachates). Gelation time is not affected  
503 by additive content, therefore the amount of UV dose can be kept to a minimum. Porous  
504 structure resulting from diazirine photolysis/nitrogen generation reduces the stiffness of the  
505 matrix, but can be beneficial in two ways: first, access is available for bone growth through  
506 the matrix, and second, the expansion of matrix allows the adhesive to fill implant/tissue gaps  
507 more efficiently. These advantages are not without drawbacks; as the effectiveness of UV  
508 curing is decreasing with thickness, care should be taken when applying adhesive to avoid  
509 incomplete curing. The resulting implant adhesion (shear) strength remains to be improved  
510 by a factor of 10 – 100x for load bearing applications, but may meet less strenuous, non-  
511 loading bearing applications. Our future work will continue to improve the adhesion strength  
512 of light activated bone implants while expanding the technology to the latest materials  
513 available for transparent waveguides.<sup>46-48</sup>

514 *In vivo* investigation of CaproGlu has previously demonstrated moderate immunological  
515 response<sup>16</sup>. CaproGlu was also assessed by OECD-regulated *in vitro* tests that demonstrated  
516 no sensitization or genotoxic effect.<sup>17</sup> CaproGlu is polycaprolactone-based crosslinked  
517 material that is biodegradable like its predecessors: the family of biodegradable polymers  
518 with well-defined degradation mechanism (ester hydrolysis flushed through metabolic  
519 pathways) and the range of different degradation kinetics based on crosslinking density (i.e.  
520 polymerization time, molecular weight).<sup>33, 49-50</sup> In our previous *in vivo* work (rabbit model)  
521 we have observed CaproGlu resorption within 1-3 weeks due to the porous nature of UVA-  
522 activated CaproGlu bioadhesive layer in close contact with blood vessels.<sup>16</sup> Like all  
523 biodegradable materials, the degradation kinetics of CaproGlu biocomposite is anticipated to

524 be dependent on several factors, including the parameters reported in this paper:  
525 concentration / size / type of solid bioactive particles as well as the crosslinking density  
526 dependent on CaproGlu molecular weight / diazirine grafting percentage / UVA energy dose.  
527 Dedicated biodegradation study is currently conducted in our laboratory and the results will  
528 be reported in future.

529

## 530 **5. Conclusion**

531 A unique strategy of bone fixation by UV light activation of transparent biopolymers is  
532 demonstrated through the unique CaproGlu biocomposites. CaproGlu-based biocomposites  
533 combination of rapid expansion and interfacial crosslinking provide a less traumatic method  
534 of bone implant fixation compared to metal pins or screws. When mixed with bioactive solid  
535 additives, liquid CaproGlu yields composites that have tunable mechanical properties  
536 controlled by; (i) concentration of solid particles in the composite; (ii) particle size; and (iii)  
537 joules light dose. The synthetic nature of CaproGlu, straight-forward production of  
538 composites by simple mixing, interfacial sustainability to applied mechanical load and non-  
539 invasive crosslinking strategy, opens a pathway for future bone fixation devices based on  
540 transparent biopolymers.

541

## 542 **ASSOCIATED CONTENT**

### 543 **Supporting Information**

544 Supporting information contains the extended photorheometry data (**Fig. S1-S3; Table S1**),  
545 pore size distribution measured from SEM images (**Fig. S4**) and EDX results (**Table S2**).

546

547

548 **AUTHOR INFORMATION**

549 **Author Contributions**

550 The manuscript was produced through contributions from all listed authors. The final version  
551 of the manuscript is approved by all listed authors.

552 **DECLARATION OF CONFLICT OF INTEREST**

553 T.W.J. Steele and I. Djordjevic are co-inventors of patent application: Hygroscopic, Cross-  
554 linking Coatings and Bioadhesives; PCT/SG2018/050452. Authors declare no competing  
555 interests.

556 **FUNDING SOURCES**

557 Ministry of Education Tier 1 Grant RG17/18 (S): Novel light activated, diazo protecting  
558 groups, Ministry of Education Tier 2 Grant (MOE2018-T2-2-114): CaproGlu, Double sided  
559 wet-tissue adhesives, NTUitive POC (Gap) Fund NGF/2018/05: Aesthetic Applications of  
560 CaproGlu Bioadhesives, and A\*Star IAF PP Grant (H19/01/a0/0II9): CathoGlu  
561 Bioadhesives-preventing catheter extravasation and skin infections.

562 **References**

- 563 1. Lopes, D.; Martins-Cruz, C.; Oliveira, M. B.; Mano, J. F., Bone physiology as  
564 inspiration for tissue regenerative therapies. *Biomaterials* **2018**, *185*, 240-275.
- 565 2. Dan Wang, J. R. G., Xu Zhang, Bingkun Zhao, Dai Fei Elmer Ker, and Gregory M.  
566 Cooper, Calvarial Versus Long Bone: Implications for Tailoring Skeletal Tissue Engineering.  
567 *Tissue Engineering Part B: Reviews* **2020**, *26* (1), 46-63.
- 568 3. Christel, P.; Cerf, G.; Pilla, A., Time evolution of the mechanical properties of the  
569 callus of fresh fractures. *Annals of Biomedical Engineering* **1981**, *9* (4), 383-391.
- 570 4. Bahney, C. S.; Zondervan, R. L.; Allison, P.; Theologis, A.; Ashley, J. W.; Ahn, J.;  
571 Miclau, T.; Marcucio, R. S.; Hankenson, K. D., Cellular biology of fracture healing. *J Orthop*  
572 *Res* **2019**, *37* (1), 35-50.
- 573 5. Suzuki, T.; Matsuura, Y.; Yamazaki, T.; Akasaka, T.; Ozone, E.; Matsuyama, Y.;  
574 Mukai, M.; Ohara, T.; Wakita, H.; Taniguchi, S.; Ohtori, S., Biomechanics of callus in the  
575 bone healing process, determined by specimen-specific finite element analysis. *Bone* **2020**,  
576 *132*, 115212.

- 577 6. Richardson, J.; Cunningham, J.; Goodship, A.; O'connor, B.; Kenwright, J.,  
578 Measuring stiffness can define healing of tibial fractures. *The Journal of bone and joint*  
579 *surgery. British volume* **1994**, *76* (3), 389-394.
- 580 7. Kim, H.-J.; Chang, S.-H.; Jung, H.-J., The simulation of tissue differentiation at a  
581 fracture gap using a mechano-regulation theory dealing with deviatoric strains in the presence  
582 of a composite bone plate. *Composites Part B: Engineering* **2012**, *43* (3), 978-987.
- 583 8. Shah, F. A.; Ruscsák, K.; Palmquist, A., 50 years of scanning electron microscopy of  
584 bone—a comprehensive overview of the important discoveries made and insights gained into  
585 bone material properties in health, disease, and taphonomy. *Bone Research* **2019**, *7* (1), 15.
- 586 9. Stahel, P. F.; Alfonso, N. A.; Henderson, C.; Baldini, T., Introducing the “Bone-  
587 Screw-Fastener” for improved screw fixation in orthopedic surgery: a revolutionary paradigm  
588 shift? *Patient Safety in Surgery* **2017**, *11* (1), 6.
- 589 10. Bali, R. K.; Sharma, P.; Jindal, S.; Gaba, S., To evaluate the efficacy of biodegradable  
590 plating system for fixation of maxillofacial fractures: A prospective study. *Natl J Maxillofac*  
591 *Surg* **2013**, *4* (2), 167-172.
- 592 11. Degala, S.; Shetty, S.; Ramya, S., Fixation of zygomatic and mandibular fractures  
593 with biodegradable plates. *Ann Maxillofac Surg* **2013**, *3* (1), 25-30.
- 594 12. Ali, A. A. A.; Kabbash, M. M.; Said, S. M. A.; Shoeib, M. A.; Osman, M. H., Use of  
595 biodegradable plates and screws in the treatment of pediatric facial bone fractures. *Egyptian*  
596 *Journal of Oral & Maxillofacial Surgery* **2016**, *7* (3), 86-93.
- 597 13. Seen, S.; Young, S. M.; Teo, S. J.; Lang, S. S.; Amrith, S.; Lim, T. C.; Sundar, G.,  
598 Permanent Versus Bioresorbable Implants in Orbital Floor Blowout Fractures. *Ophthalmic*  
599 *plastic and reconstructive surgery* **2018**, *34* (6), 536-543.
- 600 14. Yi, H.; Ur Rehman, F.; Zhao, C.; Liu, B.; He, N., Recent advances in nano scaffolds  
601 for bone repair. *Bone Research* **2016**, *4* (1), 16050.
- 602 15. Steiner, J. A.; Ferguson, S. J.; van Lenthe, G. H., Screw insertion in trabecular bone  
603 causes peri-implant bone damage. *Medical engineering & physics* **2016**, *38* (4), 417-22.
- 604 16. Djordjevic, I.; Pokhonenko, O.; Shah, A. H.; Wicaksono, G.; Blancafort, L.; Hanna, J.  
605 V.; Page, S. J.; Nanda, H. S.; Ong, C. B.; Chung, S. R.; Chin, A. Y. H.; McGrouther, D.;  
606 Choudhury, M. M.; Li, F.; Teo, J. S.; Lee, L. S.; Steele, T. W. J., CaproGlu: Multifunctional  
607 tissue adhesive platform. *Biomaterials* **2020**, *260*, 120215.
- 608 17. Djordjevic, I.; Wicaksono, G.; Solic, I.; Steele, T. W., In Vitro Biocompatibility of  
609 Diazirine - Grafted Biomaterials. *Macromolecular Rapid Communications* **2020**, 2000235.
- 610 18. Steele, T. W. J.; Djordjevic, I., HYGROSCOPIC, CROSSLINKING COATINGS  
611 AND BIOADHESIVES, PCT/SG2018/050452. *PCT/SG2018/050452* **2019**.
- 612 19. Shah, A.; Pilla, K.; Gandhi, P.; Jonnalagadda, K.; Steele, T., Pulsed Laser Activation  
613 of Carbene Bioadhesive Boosts Bonding Strength. *Macromolecular Materials and*  
614 *Engineering*. **2019**, Accepted.
- 615 20. Gareb, B.; Roossien, C. C.; van Bakelen, N. B.; Verkerke, G. J.; Vissink, A.; Bos, R.  
616 R. M.; van Minnen, B., Comparison of the mechanical properties of biodegradable and  
617 titanium osteosynthesis systems used in oral and maxillofacial surgery. *Scientific Reports*  
618 **2020**, *10* (1), 18143.
- 619 21. Mehra, R., Application of refractive index mixing rules in binary systems of  
620 hexadecane and heptadecane withn-alkanols at different temperatures. *Journal of Chemical*  
621 *Sciences* **2003**, *115* (2), 147-154.
- 622 22. Baino, F.; Fiume, E., Quantifying the effect of particle size on the crystallization of  
623 45S5 bioactive glass. *Materials Letters* **2018**, *224*, 54-58.
- 624 23. Fiume, E.; Barberi, J.; Verné, E.; Baino, F., Bioactive Glasses: From Parent 45S5  
625 Composition to Scaffold-Assisted Tissue-Healing Therapies. *Journal of Functional*  
626 *Biomaterials* **2018**, *9* (1).

- 627 24. Baino, F.; Verné, E.; Fiume, E.; Peitl, O.; Zanotto, E. D.; Brandão, S. M.; Schellini, S.  
628 A., Bioactive glass and glass-ceramic orbital implants. *International Journal of Applied*  
629 *Ceramic Technology* **2019**, *16* (5), 1850-1863.
- 630 25. Kargozar, S.; Kermani, F.; Mollazadeh Beidokhti, S.; Hamzehlou, S.; Verné, E.;  
631 Ferraris, S.; Baino, F., Functionalization and Surface Modifications of Bioactive Glasses  
632 (BGs): Tailoring of the Biological Response Working on the Outermost Surface Layer.  
633 *Materials* **2019**, *12* (22).
- 634 26. Ali, U.; Karim, K. J. B. A.; Buang, N. A., A Review of the Properties and  
635 Applications of Poly (Methyl Methacrylate) (PMMA). *Polymer Reviews* **2015**, *55* (4), 678-  
636 705.
- 637 27. Peters, K., Polymer optical fiber sensors—a review. *Smart Materials and Structures*  
638 **2010**, *20* (1), 013002.
- 639 28. Motherway, J. A.; Verschueren, P.; Van der Perre, G.; Vander Sloten, J.; Gilchrist, M.  
640 D., The mechanical properties of cranial bone: The effect of loading rate and cranial sampling  
641 position. *Journal of Biomechanics* **2009**, *42* (13), 2129-2135.
- 642 29. Djordjevic, I.; Wicaksono, G.; Solic, I.; Steele, T. W. J., Diazoalkane decay kinetics  
643 from UVA-active protein labelling molecules: Trifluoromethyl phenyl diazirines. *Results in*  
644 *Chemistry* **2020**, *2*, 100066.
- 645 30. Reis, J. C. R.; Lampreia, I. M. S.; Santos, Â. F. S.; Moita, M. L. C. J.; Douh eret, G.,  
646 Refractive Index of Liquid Mixtures: Theory and Experiment. *ChemPhysChem* **2010**, *11* (17),  
647 3722-3733.
- 648 31. Nizamoglu, S.; Gather, M. C.; Humar, M.; Choi, M.; Kim, S.; Kim, K. S.; Hahn, S.  
649 K.; Scarcelli, G.; Randolph, M.; Redmond, R. W., Bioabsorbable polymer optical waveguides  
650 for deep-tissue photomedicine. *Nature communications* **2016**, *7*.
- 651 32. Turvey, T. A.; Proffit, W. P.; Phillips, C., Biodegradable fixation for  
652 craniomaxillofacial surgery: a 10-year experience involving 761 operations and 745 patients.  
653 *Int J Oral Maxillofac Surg* **2011**, *40* (3), 244-249.
- 654 33. Abrisham, M.; Noroozi, M.; Panahi-Sarmad, M.; Arjmand, M.; Goodarzi, V.; Shakeri,  
655 Y.; Golbaten-Mofrad, H.; Dehghan, P.; Seyfi Sahzabi, A.; Sadri, M.; Uzun, L., The role of  
656 polycaprolactone-triol (PCL-T) in biomedical applications: A state-of-the-art review.  
657 *European Polymer Journal* **2020**, *131*, 109701.
- 658 34. Shah, A. H.; Pokholenko, O.; Nanda, H. S.; Steele, T. W. J., Non-aqueous, tissue  
659 compliant carbene-crosslinking bioadhesives. *Materials Science and Engineering: C* **2019**,  
660 *100*, 215-225.
- 661 35. Kim, Y.-T.; Hitchcock, R. W.; Bridge, M. J.; Tresco, P. A., Chronic response of adult  
662 rat brain tissue to implants anchored to the skull. *Biomaterials* **2004**, *25* (12), 2229-2237.
- 663 36. Wicaksono, G.; Djordjevic, I.; Shah, A. H.; Steele, T. W. J., Photocrosslinking of  
664 bioadhesive dendrimer polycaprolactone composites. *Polymer Testing* **2019**, *80*, 106099.
- 665 37. Barralet, J. E.; Duncan, C. O.; Dover, M. S.; Bassett, D. C.; Nishikawa, H.; Monaghan,  
666 A.; Gbureck, U., Cortical bone screw fixation in ionically modified apatite cements. *Journal*  
667 *of Biomedical Materials Research Part B: Applied Biomaterials* **2005**, *73B* (2), 238-243.
- 668 38. Cavalu, S., Acrylic Bone Cements: New Insight and Future Perspective. *Key*  
669 *Engineering Materials* **2017**, *745*, 39-49.
- 670 39. Lee, C. M.; Engelbrecht, C. J.; Soper, T. D.; Helmchen, F.; Seibel, E. J., Scanning  
671 fiber endoscopy with highly flexible, 1-mm catheterscopes for wide-field, full-color imaging.  
672 *Journal of biophotonics* **2010**, *3* (5-6), 385.
- 673 40. Bistolfi, A.; Ferracini, R.; Albanese, C.; Vern e, E.; Miola, M., PMMA-Based Bone  
674 Cements and the Problem of Joint Arthroplasty Infections: Status and New Perspectives.  
675 *Materials (Basel)* **2019**, *12* (23), 4002.

- 676 41. Saleh, K. J.; El Othmani, M. M.; Tzeng, T. H.; Mihalko, W. M.; Chambers, M. C.;  
677 Grupp, T. M., Acrylic bone cement in total joint arthroplasty: A review. *Journal of*  
678 *Orthopaedic Research* **2016**, *34* (5), 737-744.
- 679 42. Kawashita, M.; Kawamura, K.; Li, Z., PMMA-based bone cements containing  
680 magnetite particles for the hyperthermia of cancer. *Acta Biomaterialia* **2010**, *6* (8), 3187-  
681 3192.
- 682 43. Juvonen, T.; Nuutinen, J.-P.; Koistinen, A. P.; Kröger, H.; Lappalainen, R.,  
683 Biomechanical evaluation of bone screw fixation with a novel bone cement. *BioMedical*  
684 *Engineering OnLine* **2015**, *14* (1), 74.
- 685 44. Yousefi, A.-M., A review of calcium phosphate cements and acrylic bone cements as  
686 injectable materials for bone repair and implant fixation. *Journal of Applied Biomaterials &*  
687 *Functional Materials* **2019**, *17* (4), 2280800019872594.
- 688 45. Sánchez-Fernández, M. J.; Hammoudeh, H.; Félix Lanao, R. P.; van Erk, M.; van  
689 Hest, J. C. M.; Leeuwenburgh, S. C. G., Bone-Adhesive Materials: Clinical Requirements,  
690 Mechanisms of Action, and Future Perspective. *Advanced Materials Interfaces* **2019**, *6* (4),  
691 1802021.
- 692 46. Farajikhah, S.; Runge, A. F. J.; Boumelhem, B. B.; Rukhlenko, I. D.; Stefani, A.;  
693 Sayyar, S.; Innis, P. C.; Fraser, S. T.; Fleming, S.; Large, M. C. J., Thermally drawn  
694 biodegradable fibers with tailored topography for biomedical applications. *Journal of*  
695 *Biomedical Materials Research Part B: Applied Biomaterials* **2021**, *109* (5), 733-743.
- 696 47. Prajzler, V.; Arif, S.; Min, K.; Kim, S.; Někvindova, P., All-polymer silk-fibroin  
697 optical planar waveguides. *Optical Materials* **2021**, *114*, 110932.
- 698 48. Rezapour Sarabi, M.; Jiang, N.; Ozturk, E.; Yetisen, A. K.; Tasoglu, S., Biomedical  
699 optical fibers. *Lab on a Chip* **2021**, *21* (4), 627-640.
- 700 49. Woodruff, M. A.; Hutmacher, D. W., The return of a forgotten polymer—  
701 Polycaprolactone in the 21st century. *Progress in polymer science* **2010**, *35* (10), 1217-1256.
- 702 50. Lam, C. X.; Savalani, M. M.; Teoh, S.-H.; Hutmacher, D. W., Dynamics of in vitro  
703 polymer degradation of polycaprolactone-based scaffolds: accelerated versus simulated  
704 physiological conditions. *Biomedical materials* **2008**, *3* (3), 034108.

705